Buckling between soft walls: sequential stabilisation through contact

Zhenkui Wang[a,b], G.H.M. van der Heijden[b,*]

[a] State Key Laboratory of Hydraulic Engineering Simulation and Safety, Tianjin University, Tianjin 300072, China

[b] Department of Civil, Environmental and Geomatic Engineering, University College London, London WC1E 6BT, UK

Corresponding author: G.H.M. van der Heijden, g.heijden@ucl.ac.uk

Abstract:

Motivated by applications of soft contact problems such as guidewires used in medical and engineering applications, we consider a compressed rod deforming between two parallel elastic walls. Free elastica buckling modes other than the first are known to be unstable. We find the soft constraining walls to have the effect of sequentially stabilising higher modes in multiple contact by a series of bifurcations in each of which the degree of instability (the index) is decreased by one. Further symmetry-breaking bifurcations in the stabilisation process generate solutions with different contact patterns that allow for a classification in terms of binary symbol sequences. In the hard-contact limit all these bifurcations collapse into highly-degenerate 'contact bifurcations'. For any given wall separation at most a finite number of modes can be stabilised and eventually, under large enough compression, the rod jumps into the inverted straight state. We chart the sequence of events, under increasing compression, leading from the initial straight state in compression to the final straight state in tension, in effect the process of pushing a rod through a cavity. Our results also give new insight into universal features of symmetry-breaking in higher-mode elastic deformations.

We present this study also as a showcase for a practical approach to stability analysis based on numerical bifurcation theory and without the intimidating mathematical technicalities often accompanying stability analysis in the literature. The method delivers the stability index and can be straightforwardly applied to other elastic stability problems.

Keywords: Buckling; Constrained beam; Winkler foundation; Large deformation; Bifurcation; Symmetry-breaking; Stability.

1. Introduction

Laterally constrained buckling of a slender elastic structure occurs in various areas of technology. In medicine guidewires are used for the recanalisation of arteries or veins (Alderliesten et al., 2006). When compression is applied to traverse an occluded vascular section the wire may be pushed into the blood vessel wall impairing the surgeon's ability to steer the wire. In oil-well drilling the drill string may make contact with the borehole wall due to its own weight or as a result of axial loads, especially in horizontal drilling (Gao and Huang, 2015; Tan and Forsman, 1995). Similar buckling problems are encountered in the borescopic or soft robotic examination of pipe or tube systems (Gilbertson et al., 2017; Wang and Yamamoto, 2017; Yeh et al., 2019).

Although all these problems occur in a three-dimensional setting, the buckling problem under compressive load is essentially a two-dimensional problem with the rod bouncing between opposite sides of the clearance, provided we can ignore out-of-plane instabilities (one can also consider compressed strips, plates or sheets between two walls (Roman and Pocheau, 2002) in which case any out-of-plane instability will be suppressed).

If the constraining walls are stiff relative to the forces applied, the problem can be studied as a hard-contact problem with rigid walls. Bilateral rigid walls have been studied extensively. Feodosiev (1977) solves the problem using linear small-deformation theory. In subsequent work by Domokos et al. (1997), Chai (1998) and Roman & Pocheau (2002) a geometrically-exact large-deformation analysis is given based on the Euler elastica; experiments are performed as well. These studies find that point contact grows into line contact at a critical load followed by secondary buckling away from the wall under a falling load, eventually leading to contact with the opposite wall. The point of secondary buckling represents a local maximum (a fold in bifurcation terms) for the compressive load in the load-displacement diagram.

Variations of this hard-contact problem have also been studied. In (Katz and Givli, 2015) rigid walls are considered, but one of the walls is mounted on a spring. Rigid but curved walls are treated in (Chen and Hung, 2014).

Soft contact is considered in (Chen and Wen, 2019) where a rod is compressed between two parallel flexible walls of Winkler type. Using small-deformation (linear) theory, the authors show that, at least for the relatively small wall-to-wall distance and relatively large wall stiffness considered, the compressive load keeps rising through secondary buckling where the central section of the rod lifts off the wall leaving two bordering sections of continuous contact (see Fig. 1(b)). Eventually, however, a maximum is reached, as in the case of two rigid walls. When the load is increased past this maximum the rod is forced to jump to a remote solution. The question is: which solution?

Experiments in (Domokos et al., 1997) are for rigid (i.e., displacement-controlled) loading, but suggest that for dead (i.e., force-controlled) loading the rod would jump into a second-mode solution. A second-mode solution is unstable for a free rod, but seems somehow stabilised by contact. The precise nature of this stabilisation was not clarified in (Domokos et al., 1997) because, as the authors note, a stability analysis in the hard-contact case is problematic since the relevant functions are nonsmooth due to contact forces, rendering standard tools of stability analysis useless. In the soft-contact case, however, one gains an order of continuity as the contact force is continuous rather than a step function and one is therefore in a better position to apply a stability analysis (one is in an even better position if one replaces the walls by a potential (Manning and Bulman, 2005)). Here we identify the sequence of bifurcations that is responsible for this stabilisation through soft contact.

A full elucidation of the various jump phenomena under either dead or rigid loading requires a nonlinear large-deformation study. We use the geometrically-exact Euler elastica model for the structure and, following (Chen and Wen, 2019), a linear Winkler model for contact. We find various other nonlinear phenomena in addition to stabilisation of higher modes. For instance, there are several types of symmetry-breaking bifurcation leading to nonsymmetric solutions absent from a linear study. The existence of multiple solutions necessitates a stability analysis to determine which branches are stable and therefore physically relevant (perhaps as destinations of a jump at a fold). We present a stability analysis based on numerical bifurcation theory without the often intimidating mathematical technicalities accompanying stability analyses in the literature.

The structure of the paper is as follows. In Section 2 we present the constrained elastica model. In Section 3 we discuss load-displacement diagrams for different wall separations. We identify various jump scenarios and show that for walls at smaller separation jumps into higher modes may occur. In Section 4 we present our stability approach and identify the stable solution branches. Section 5 takes a closer look at the organisation of solution branches near initial contact and how stability is reached as the combined effect of a sequence of bifurcations. In Section 6 we briefly discuss the role of the wall stiffness in the various nonlinear phenomena and Section 7 closes the paper with a discussion of our results.

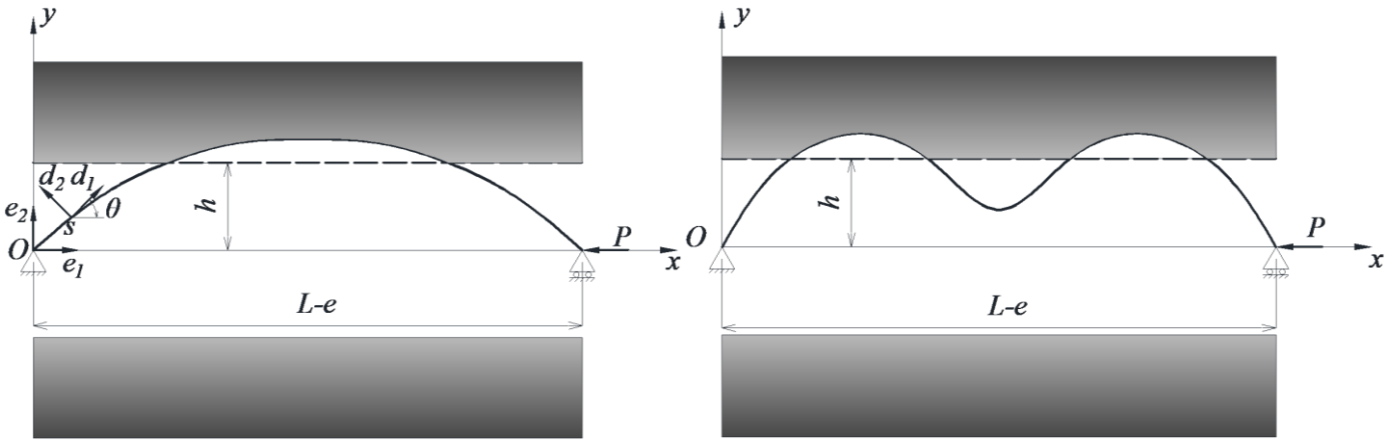

(a) (b)

Fig. 1 A pinned-pinned buckled beam constrained by a pair of elastic walls. (a) One-segment line contact. (b) Two-segment line contact.

2. Mathematical modelling

We consider an intrinsically straight uniform rod placed symmetrically between two parallel horizontal walls. The ends of the rod are pin-supported with the right end free to slide in under the action of a horizontal compressive load P (see Fig. 1(a)). The rod is taken to be linearly elastic, inextensible and unshearable and the walls are also linearly elastic, of Winkler type.

Only planar deformation is considered but of course the model also describes laterally-uniform deformations of a uniaxially loaded plate.

Let $\{\boldsymbol{e}_1, \boldsymbol{e}_2\}$ be the unit-vector frame of a fixed Cartesian coordinate system with origin O at the left end of the rod and with $\boldsymbol{e}_1$ directed parallel to the walls. The centreline of the rod can then be written as $\boldsymbol{r}(s) = x(s)\,\boldsymbol{e}_1 + y(s)\,\boldsymbol{e}_2$, where s is arclength along the rod, measured from O. To describe the configuration of the rod we also introduce an orthonormal material or body frame $\{\boldsymbol{d}_1, \boldsymbol{d}_2\}$ with the vector $\boldsymbol{d}_1$ taken tangent to the beam, i.e. we have $\boldsymbol{d}_1 = \dot{\boldsymbol{r}}$, where the overdot denotes differentiation with respect to s (see Fig. 1(a)). Denoting the angle between the tangent $\boldsymbol{d}_1$ and the horizontal by θ, the relationship between the fixed and body frames can be written as

$$\begin{cases} \boldsymbol{d}_1 = \cos\theta\,\boldsymbol{e}_1 + \sin\theta\,\boldsymbol{e}_2 \\ \boldsymbol{d}_2 = -\sin\theta\,\boldsymbol{e}_1 + \cos\theta\,\boldsymbol{e}_2 \end{cases} \tag{1}$$

from which it immediately follows that

$$\begin{cases} \dot{x} = \cos\theta \\ \dot{y} = \sin\theta \end{cases} \tag{2}$$

Denoting internal forces and moments along the rod by $\boldsymbol{F} = F_x\boldsymbol{e}_1 + F_y\boldsymbol{e}_2$ and $\boldsymbol{M} = M\boldsymbol{e}_1 \times \boldsymbol{e}_2$, respectively, the equilibrium equations of the rod are given by (Antman, 1995; van der Heijden, 2001):

$$\begin{cases} \dot{\boldsymbol{F}} + \boldsymbol{f} = \boldsymbol{0} \\ \dot{M}\boldsymbol{e}_1 \times \boldsymbol{e}_2 + \dot{\boldsymbol{r}} \times \boldsymbol{F} = \boldsymbol{0} \end{cases} \tag{3}$$

where $\boldsymbol{f} = f\boldsymbol{e}_2 = -\beta Z(s)(|y| - h)\boldsymbol{e}_2$ is the external distributed contact force from the two walls. Here h is half the wall-to-wall separation and $Z(s)$ is a contact function describing the constraining character of the walls, here defined as $Z(s) = 1$ if $y(s) \geq h$, $Z(s) = -1$ if $y(s) \leq -h$ and $Z(s) = 0$ if $|y(s)| < h$, while β is the stiffness of the walls. In components, Eq. (3) reads

$$\dot{F}_x = 0 \tag{4}$$

$$\dot{F}_y = \beta Z(s)(|y| - h) \tag{5}$$

$$\dot{M} - F_x\sin\theta + F_y\cos\theta = 0 \tag{6}$$

From Eq. (4), $F_x = -P$, where P is the applied end compressive force. With the constitutive relation $M = EI\dot{\theta}$, where E is Young's modulus of the material and I is the second moment of area of the rod's cross-section (both assumed to be constant), Eq. (6) then gives

$$EI\ddot{\theta} + P\sin\theta + F_y\cos\theta = 0 \tag{7}$$

In the case of a free rod $\beta = 0$ and if no shear force is present ($F_y = 0$), we obtain

$$EI\ddot{\theta} + P\sin\theta = 0 \tag{8}$$

i.e., the Euler elastica.

Linearisation of Eq. (7), valid for small deformations (i.e., $\theta \ll 1$ and hence $\theta \approx \frac{\mathrm{d}y}{\mathrm{d}x} = y_{,x}$), gives, on using Eq. (5),

$$EIy_{,xxxx} + Py_{,xx} + \beta Z(x)(|y| - h) = 0 \tag{9}$$

which is the equation studied in (Chen and Wen, 2019).

The pinned ends at $s = 0$ and $s = L$, L being the length of the rod, imply the five boundary conditions

$$x(0) = y(0) = 0, \qquad y(L) = 0, \qquad M(0) = M(L) = 0 \tag{10}$$

for the fifth-order system of equations consisting of Eq. (2), Eq. (5) and Eq. (7) (small-deformation results can be obtained by solving the fourth-order Eq. (9) and dropping the boundary condition on x). The end shortening e can then be obtained as

$$e = L - x(L) \tag{11}$$

In the small-deformation theory this is replaced by the first-order approximation

$$e = \tfrac{1}{2}\int_0^L \left(y_{,x}\right)^2 dx \tag{12}$$

For the presentation of the numerical results in the following sections we introduce dimensionless quantities (with asterisks) according to

$$(x^*, y^*, h^*, e^*) = \frac{(x,y,h,e)}{L},\ \beta^* = \frac{\beta L^4}{EI},\ P^* = \frac{PL^2}{EI} \tag{13}$$

but, not to overburden the notation, we shall drop the asterisk (we are thus effectively working in units of L and EI).

3. Numerical results

Fig. 2 gives the load-displacement diagram for parameter values $\beta = 10^5$ and $h = 0.1$, the same values as in (Chen and Wen, 2019). (In (Chen and Chen, 2019) typical values of β for oil-well drilling are estimated to be on the order of 10^9, while for arterial stent deployment they are on the order of 10^4, from which it is concluded that in the latter case wall flexibility may need to be taken into account.) The label 'O' indicates the first-mode critical point where the straight rod first buckles. Critical loads for the elastica are given by $P = n^2\pi^2$, where n is the mode number (the number of `half waves' in the post-buckling solution), so for the first mode ($n = 1$) this gives $P = \pi^2$. Further points of interest along the curve are labelled 'a', 'b', etc. with subscripts either 'l' for the exact, large-deformation, result, or 's' for the linear, small-deformation, result. Several of the corresponding solutions are illustrated in Fig. 3. (Solutions come in symmetric pairs of 'buckled-up' and 'buckled-down' solutions, originating in the supercritical pitchfork bifurcations of the straight rod at $P = n^2\pi^2$ along the vertical axis in Fig. 2. All solutions shown here and in the rest of the paper are 'buckled-up'.)

At a_l, resp. a_s first contact is made with the wall. For the linear theory this occurs at the same load as the initial buckling load, but for the exact theory this occurs at a slightly higher load. After this first contact, the load rises sharply. At b_l/b_s ($P = 8.07\pi^2$, resp. $P = 8.34\pi^2$) the midpoint of the rod first lifts off the wall in the middle, leaving wall contact in two separate segments. The loading curve reaches a maximum at c_l/c_s. Further increase of e, under falling load, leads eventually to point contact with the opposite wall (d_l/d_s). At this point all three contacts with the wall are point contacts, at zero reaction force. Indeed, points d_l/d_s lie on the third-mode elastica curve coming out of the third critical load $P = 9\pi^2$ (again, in the linear theory this midpoint contact occurs exactly at $9\pi^2$, while in the exact theory it occurs at a higher load, $P = 10.42\pi^2$). Fig. 2 also shows a branch of nonsymmetric solutions only present in the nonlinear model.

Also shown in Fig. 2 is the curve of second-mode solutions. It can be deduced from the figure that under dead loading (P control) the rod goes unstable at the maximum of the loading curve, where a dynamic jump to a remote solution will occur. The figure shows that both a second-mode and a third-mode solution (g_l) are available (assuming they are stable), and possibly also a nonsymmetric solution. Hysteresis cycles (e.g., c_l-g_l-d_l-q_l) are possible if, after this jump, the load is decreased. Under rigid loading, on the other hand, no jump (and no hysteresis) is expected to occur and the rod deforms smoothly into a third mode at d_l/d_s. In the experiment in (Domokos et al., 1997), which is conducted under rigid loading, a jump into a second-mode is eventually observed, presumably because of imperfections in either the intrinsic shape of the rod or in the pinned boundary conditions.

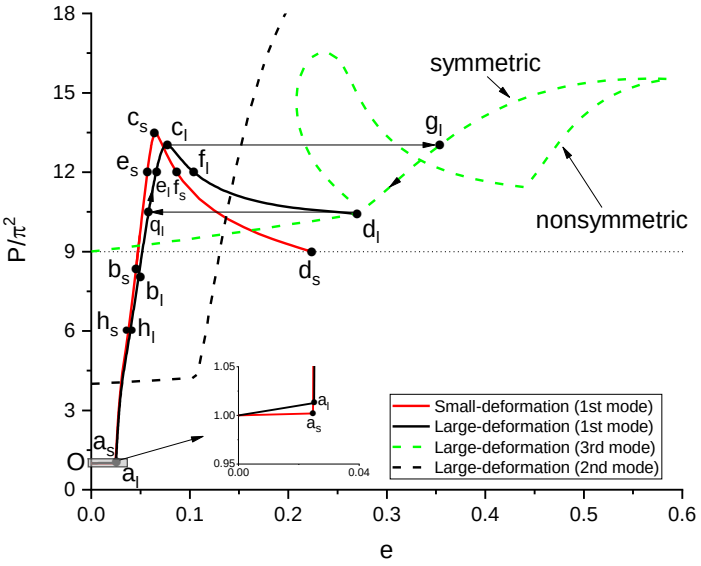

Fig. 2 Load-displacement curves for both the small- and large-deformation models. ($\beta = 10^5,\ h = 0.1$.)

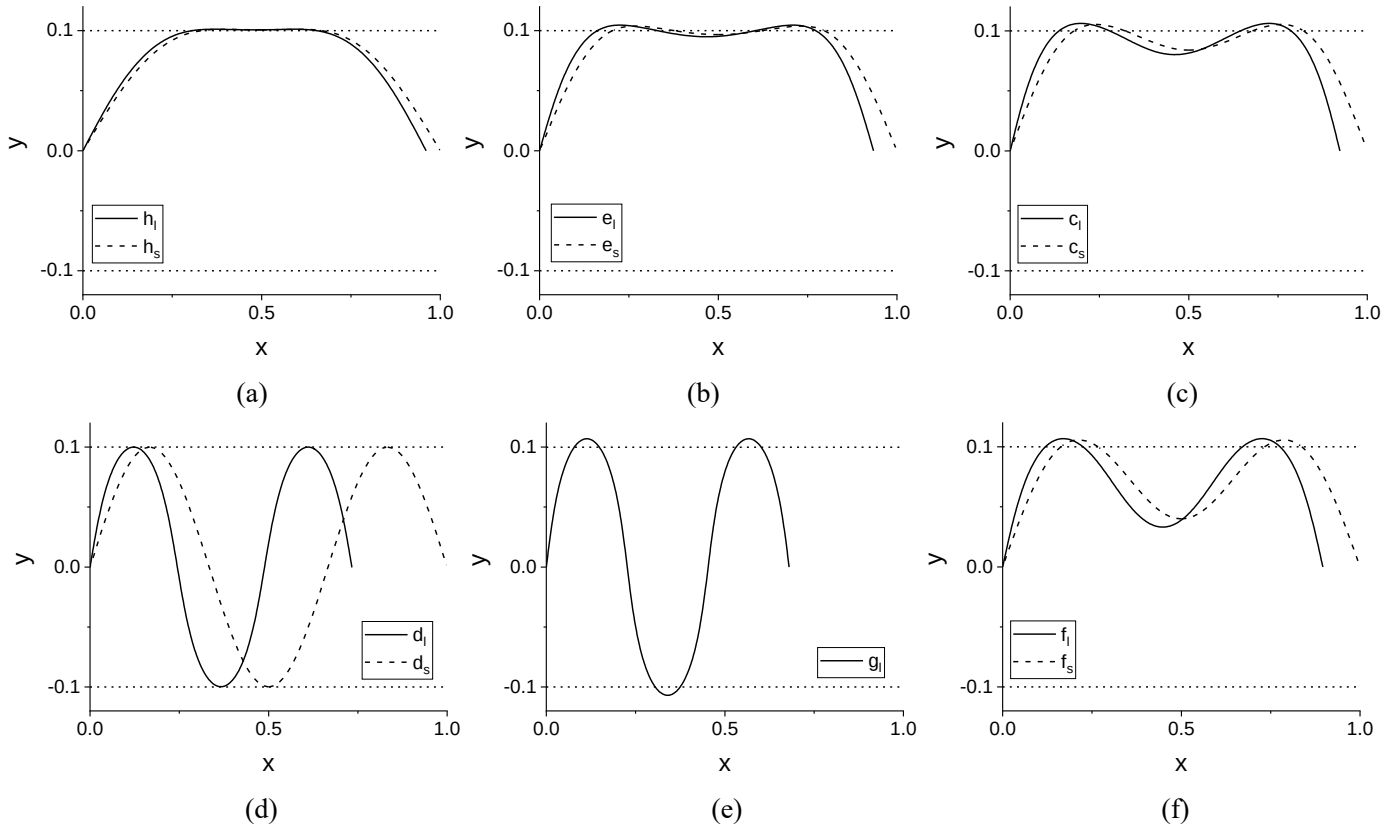

Fig. 3 Comparison of small- and large-deformation solutions at labels shown in Fig. 2. The horizontal dotted lines represent the position of the initial walls. ($\beta = 10^5,\ h = 0.1$.)

The force distributions F_y and f of solutions at points h_l and c_l are shown in Fig. 4. The plots illustrate the continuity properties of solutions: f is continuous at wall touch-down and lift-off points, but not differentiable, while F_y, as its integral, is once differentiable. This contrasts with the case of hard contact where f is a step function and F_y only continuous, with a corner (Domokos et al., 1997).

We conclude from Figs 2 and 3 that for $h = 0.1$ linear theory is reasonably accurate, predicting the same qualitative behaviour as the exact theory. This changes, however, as h is increased, i.e., when larger deformations are allowed. A first indication of this is given in Fig. 5 where the loads at point c_l/c_s and d_l/d_s are plotted. In the linear theory these loads are constant ($P = 13.4616\pi^2$, resp. $P = 9\pi^2$), independent of h (as a result of the homogeneity of the linear Eq. (9)). In the exact theory, however, the maximum load comes down, while the load at the third-mode 'landing point' d_l goes up, the two crossing over at $h = h_c = 0.1266$. This means that the jump from c_l under dead loading may be to another first mode rather than (or in addition to) a third mode, as illustrated in Fig. 6.

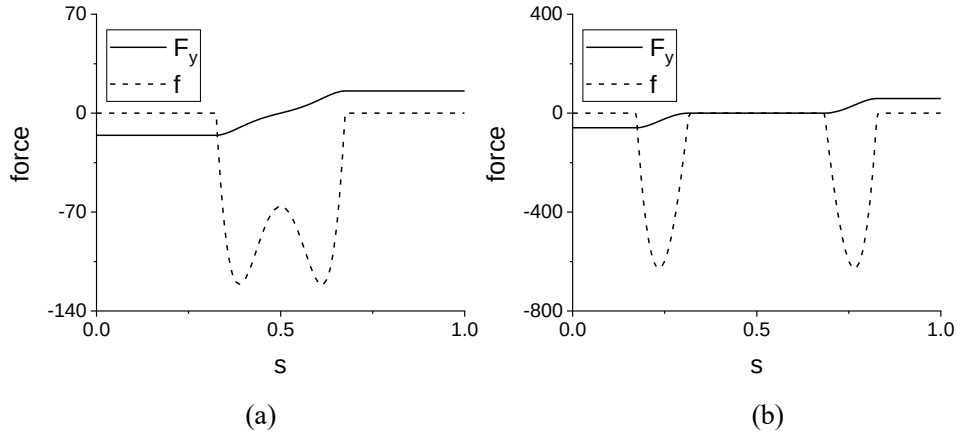

Fig. 4 Force distributions for solutions h_l (a) and c_l (b).

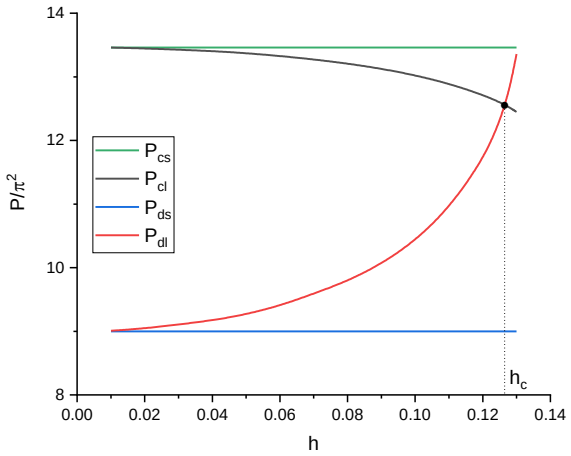

Fig. 5 Values of P_{cs}, P_{ds}, P_{cl} and P_{dl} as a function of h ($\beta = 10^5$).

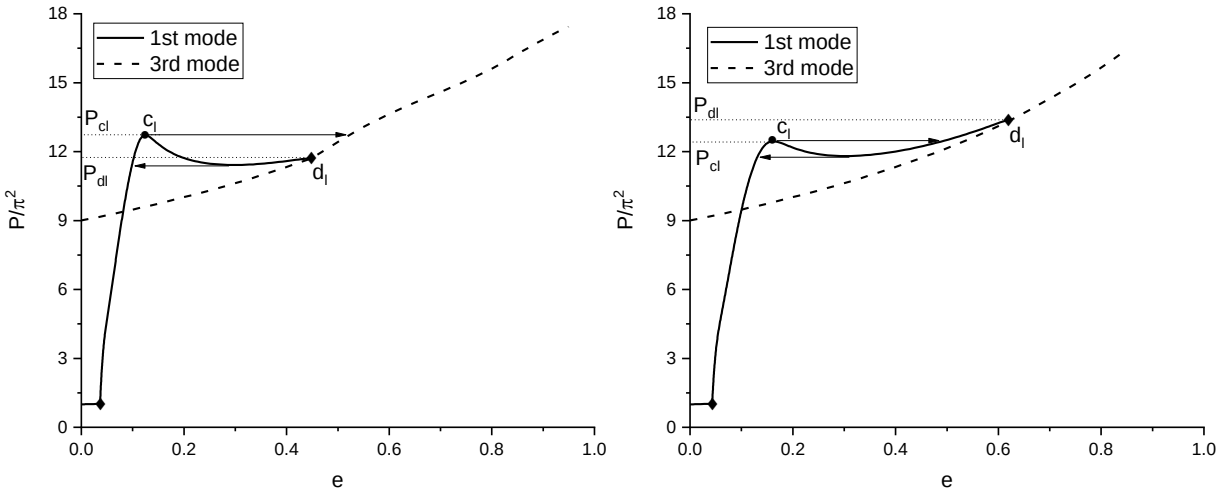

Fig. 6 Bifurcation diagrams for h close to h_c (a) $h = 0.12$. (b) $h = 0.13$. ($\beta = 10^5$.)

We cannot entirely rule out a jump from c_l into a third mode for $h > h_c$ because there may be additional (bifurcating) solution branches not included in Fig. 6(b). However, rigorous upper bounds on h for the existence of a jump into a third, and any other, mode can be computed as follows. From the exact elastica solution (Love, 1892) the maximum deflection of a free rod is determined by the condition

$$E(k) - 2(1-k^2)K(k) = 0$$

where K and E are the complete elliptic integrals of the first and second kind, respectively, and k is the elliptic modulus (related to the end angle $\theta(L)$). This gives the critical value $k = k_c = 0.837453$. The maximum deflection of the nth mode is then

$$y_{m,n} = \frac{k_c}{nK(k_c)}$$

Thus the critical h values for the first four modes are ($h_n = y_{m,n}$):

$$h_1 = 0.403140, \quad h_2 = 0.201570, \quad h_3 = 0.134380 \quad \text{and} \quad h_4 = 0.100785.$$

This means that for $h > h_3$ no third mode in wall contact can exist (i.e., there can be no 'landing point' such as d_l in Fig. 2), for $h > h_2$ no second mode in wall contact can exist, etc. The corresponding end shortening is

$$e_m = 2\left(1 - \frac{E(k_c)}{K(k_c)}\right) = 0.805310$$

independent of mode number n, while the corresponding normalised load is

$$P_{m,n} = 4n^2K(k_c)^2$$

giving the first four critical loads

$P_{m,1} = 1.7489\pi^2$, $P_{m,2} = 6.9957\pi^2$, $P_{m,3} = 15.7402\pi^2$ and $P_{m,4} = 27.9827\pi^2$.

This critical behaviour is illustrated in Fig. 6(b), which is for $h = 0.13$. Since this h is smaller than h_3 a contacting third mode still exists; it corresponds to point d_l. As h is increased this point moves up along the free third-mode curve and disappears at $(e,P) = (e_m,\ P_{m,3})$ when h reaches h_3. For larger h no contacting third mode exists and from general elastica theory we know that free modes higher than the first are unstable, so no jump or smooth transition into a third mode is possible.

For $h > h_3$ the first-mode curves detach from the third-mode curve. Out of this event comes a symmetry-breaking bifurcation, with emanating branch of nonsymmetric solutions, which rapidly moves to the left and nestles itself just to the right of the maximum as h is increased, as illustrated by the set of curves in Fig. 7. Fig. 8 compares some symmetric and nonsymmetric solutions along these curves. The second mode, not shown in Fig. 7, also interferes however and the complete picture becomes hard to interpret without a stability analysis. In the next section, therefore, we develop an approach to assess the stability of solutions, which will help to predict the actual behaviour of a rod under increasing compressive load.

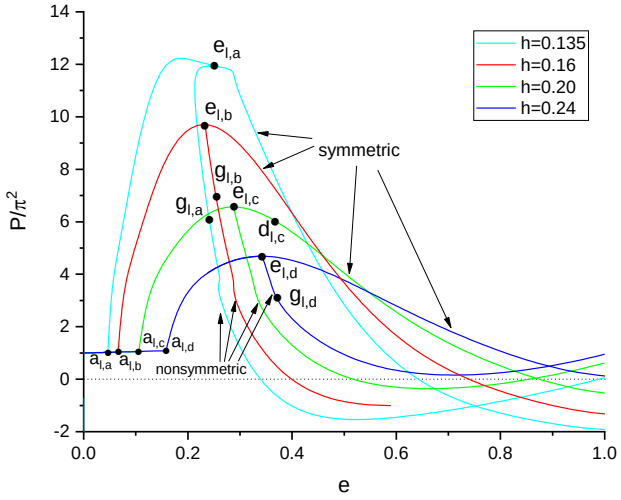

Fig. 7 First-mode bifurcation diagrams for several values of h obtained from large-deformation theory ($\beta = 10^5$).

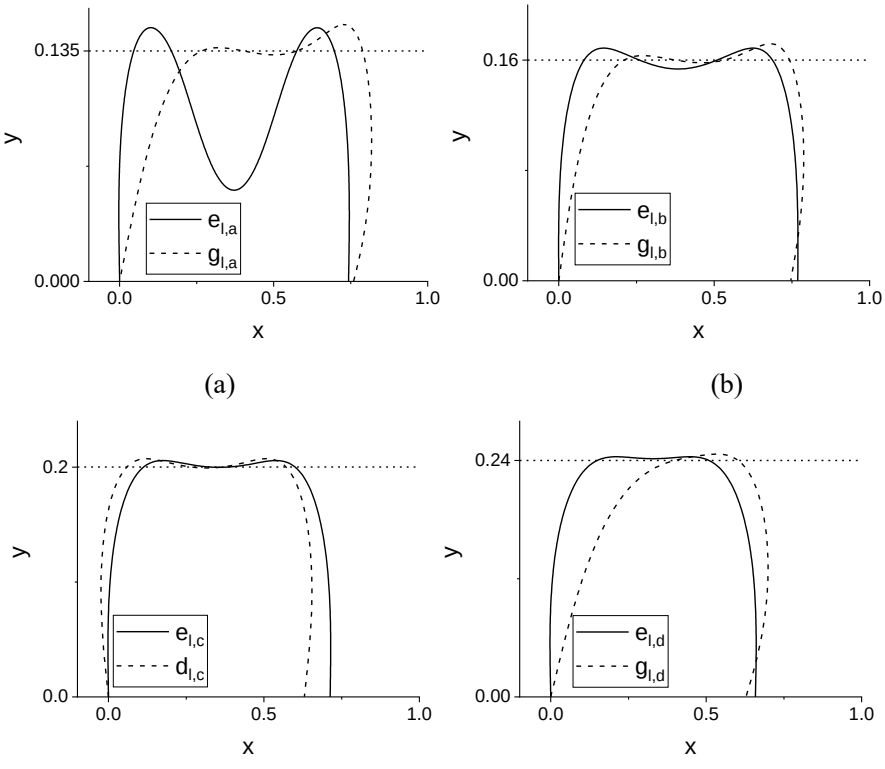

Fig. 8 Deflected rod shapes at labels shown in Fig. 7. ($\beta = 10^5$.)

4. Stability analysis

4.1 The method

We note that allowing for large deformations gives a very rich bifurcation picture. The existence of multiple solutions highlights the need for a stability analysis as some solutions may be stable while others are unstable. Normally, in such studies of the behaviour of elastic structures one can make sensible predictions about stability by appealing to generic bifurcation behaviour (or the shape of solution branches in 'distinguished' load-deflection bifurcation diagrams (van der Heijden et al., 2003), (e,P) diagrams being 'distinguished' in this sense because it is exactly e through which P does work). In a supercritical pitchfork bifurcation, for instance, generically a solution loses stability in favour of a pair of symmetry-broken solutions. Although not a rigorous approach (bifurcations may be degenerate, or may be missed in a numerical study), this in practice works very well, especially when accompanied by physical insight into the behaviour of the system under study.

However, if, as in our present case, the bifurcation diagram is very complicated this approach becomes problematic and independent confirmation of in/stability becomes necessary. Unfortunately, a rigorous approach often involves mathematical technicalities that are outside the scope of the study if one is mainly interested in the physical behaviour of the system. It is also good to realise that more rigorous approaches often need to make assumptions about the system that are difficult if not impossible to verify. For instance, the conjugate point method in the calculus of variations is a powerful method but assumes that the eigenvalues of a linear operator behave in a 'nice' way (are simple and behave monotonically under parameter change) (Manning et al., 1998). This is particularly true for problems with derivative (Neumann) boundary conditions, for which the conjugate-point method is ill-suited and a detailed knowledge of eigenvalues is still required (Manning, 2009). An application of the conjugate point method to a soft rod-wall contact problem can be seen in (Manning and Bulman, 2005), whose treatment relies heavily on the theory of linear operators in Hilbert spaces, a topic that not everyone interested in stability is prepared to delve into.

The required 'nice' properties are satisfied in the important class of Sturm-Liouville problems (i.e., boundary-value problems for second-order ODEs), but applications often fall outside this class. For instance, if one has a system of coupled Sturm-Liouville problems there are already very few general results available about the nature of its eigenvalues and the corresponding eigenfunctions (Pryce, 1993). Eigenvalues may, for example, be non-simple and cross over under parameter continuation (Chanane, 2015). Thankfully, many physically motivated problems share these 'nice' properties even though we cannot prove them. Making assumptions about eigenvalues/eigenfunctions in such cases is not much different from making assumptions about generic bifurcation behaviour.

Here we therefore develop the bifurcation approach further to obtain a practical and intuitive method of stability analysis. The method is applicable to problems with any type of boundary conditions. We start by going back to what instability really means. For a stable solution to lose stability there must exist a nearby solution (this is why stability change is closely associated with bifurcation). A nearby solution means an infinitesimally close solution, and the existence or not of such a solution is therefore governed by linearisation of the equations about the solution whose stability we are interested in. The number of unstable directions (modes) of this linearisation gives the degree of instability (the stability index), i.e., the dimension of the space of unstable small perturbations.

Thus we linearise our system of equations about a solution $(\theta,\ F_y,\ x,\ y)$ by introducing the replacements $\theta \to \theta + \varepsilon v$, $F_y \to F_y + \varepsilon f_y$ and $y \to y + \varepsilon Y$ in Eq. (2), Eq. (5) and Eq. (7), where ε is a small parameter. To first order in ε the following equations for v, f_y and Y are then obtained:

$$\begin{cases} EI\ddot{v} + P\cos\theta\, v - F_y \sin\theta\, v + \cos\theta\, f_y = 0 \\ \dot{f}_y = Z(s)\beta Y \\ \dot{Y} = \cos\theta\, v \end{cases} \tag{14}$$

with linearised boundary conditions

$$\begin{cases} \dot{v}(0) = \dot{v}(L) = 0 \\ Y(0) = Y(L) = 0 \end{cases} \tag{15}$$

Next we introduce a parameter μ in Eq. (14) as follows:

$$\begin{cases} EI\ddot{v} + \mu(P\cos\theta\, v - F_y \sin\theta\, v + \cos\theta\, f_y) = 0 \\ \dot{f}_y = Z(s)\beta Y \\ \dot{Y} = \mu\cos\theta\, v \end{cases} \tag{16}$$

μ can be thought of as a homotopy parameter: $\mu = 0$ corresponds to the unloaded rod, while $\mu = 1$ corresponds to the actual linearised system Eq. (14). Note that Eq. (15) and Eq. (16) can be written as two coupled Sturm-Liouville problems, which for $\beta = 0$ reduce to the single Sturm-Liouville problem for the elastica (Kuznetsov and Levyakov, 2002), which has all the 'nice' properties referred to above. We now let μ run from 0 to 1 and detect branching points where nontrivial solutions bifurcate from the trivial (zero) solution. The corresponding μ are the eigenvalues and the nontrivial solutions, or modes, are the eigenfunctions of the linearised equations. We thus determine how many instability-causing modes the linearised equations have and the number of branching points we pick up in this run gives the degree of instability. Note that at a bifurcation or a fold we compute an eigenvalue $\mu = 1$, i.e., eigenvalues enter or leave the unit interval through $\mu = 1$.

This approach can be regarded as an extension of the adjacent equilibrium criterion (Brush and Almroth, 1975) that goes back to Euler's study of column buckling. According to this criterion, the straight column loses stability at the first load where an infinitesimally close nontrivial solution becomes available. Although the straight solution is unstable beyond this first critical load, the adjacent equilibrium criterion can be continued to be applied as the load further increases and then detects further instabilities (of higher index) at the second, third, etc. critical loads where higher modes bifurcate.

Taking this bifurcation approach to stability, we solve the linear equations in Eq. (16) in conjunction with Eq. (2), Eq. (5) and Eq. (7), subject to boundary conditions, with the continuation and bifurcation code AUTO (Doedel et al.), using μ as a bifurcation parameter in order to detect branching points. The code allows us to switch branches at these points and to inspect the instability-causing modes (v, f_y, Y). Note that since the equations governing these modes are linear (and therefore homogeneous), the bifurcations detected are necessarily degenerate: they are 'vertical bifurcations' (Sattinger, 1971) in which the bifurcating branch of solutions has constant bifurcation parameter ($\mu = \mu_c$) and is parametrised by amplitude (or by some norm). This is not a problem for the numerical bifurcation detection. On the contrary, it is advantageous as the intersecting branches of solutions separate cleanly at right angles.

This approach is formal in the sense that no rigorous justification is given that stability changes at the branching points in the way supposed. In Euler buckling each successive pitchfork along the trivial branch adds an unstable direction; there is no branching point with a reverse pitchfork bifurcation. Physically motivated problems generally exhibit this pattern. In any case, as argued above, more sophisticated methods, apart from being much more difficult to apply, usually still have a residual element of this formality.

4.2 Results

Fig. 9 shows a more complete version of the bifurcation diagram in Fig. 2, for $h = 0.1$, with stability results included. In addition to curves of symmetric modes coming out of the critical loads $P = n^2\pi^2$ there are complicated connecting curves of symmetric (black) and nonsymmetric (red) solutions. Nonsymmetric branches connect modes 2 and 3 at first contact, while symmetric branches connect modes 1, 3 and 5 (outside the figure). Note that when the first-mode goes unstable under increasing P, both a second-mode and a third-mode solution are available as stable destinations of the dynamic jump from the fold (but none of the nonsymmetric solutions in Fig. 2). Inspecting these solutions (shown in the figure), it seems likely that the jump will take place to the third mode. This third mode, under further increase of P, will in turn go unstable at a fold at which point only a second-mode contacting solution is available. This is in fact a nonsymmetric solution as the second-mode has just undergone a symmetry-breaking bifurcation. The nonsymmetric branch can be followed a little further but eventually, at $P = 16.7600\pi^2$, another fold is reached at which point no stable contacting solution is available anymore. We must conclude that at this point the rod jumps into the straight tensile state $\theta = \pi$ (ignoring self-intersection), the only stable solution left (this solution has $e = 2$, but we indicate this transition in the figure by a horizontal arrow to the vertical axis).

It is interesting to follow events along the second-mode branch. The symmetry-breaking already mentioned is of the type in which one wave of the second-mode gradually drains into the other. Two more symmetry-breaking bifurcations occur further up the (unstable) branch. At the first, at considerably higher P, and with the waves consequently firmly pushed into the walls, the segments in contact themselves break symmetry (again, much like two 'waves' draining into one), but overall

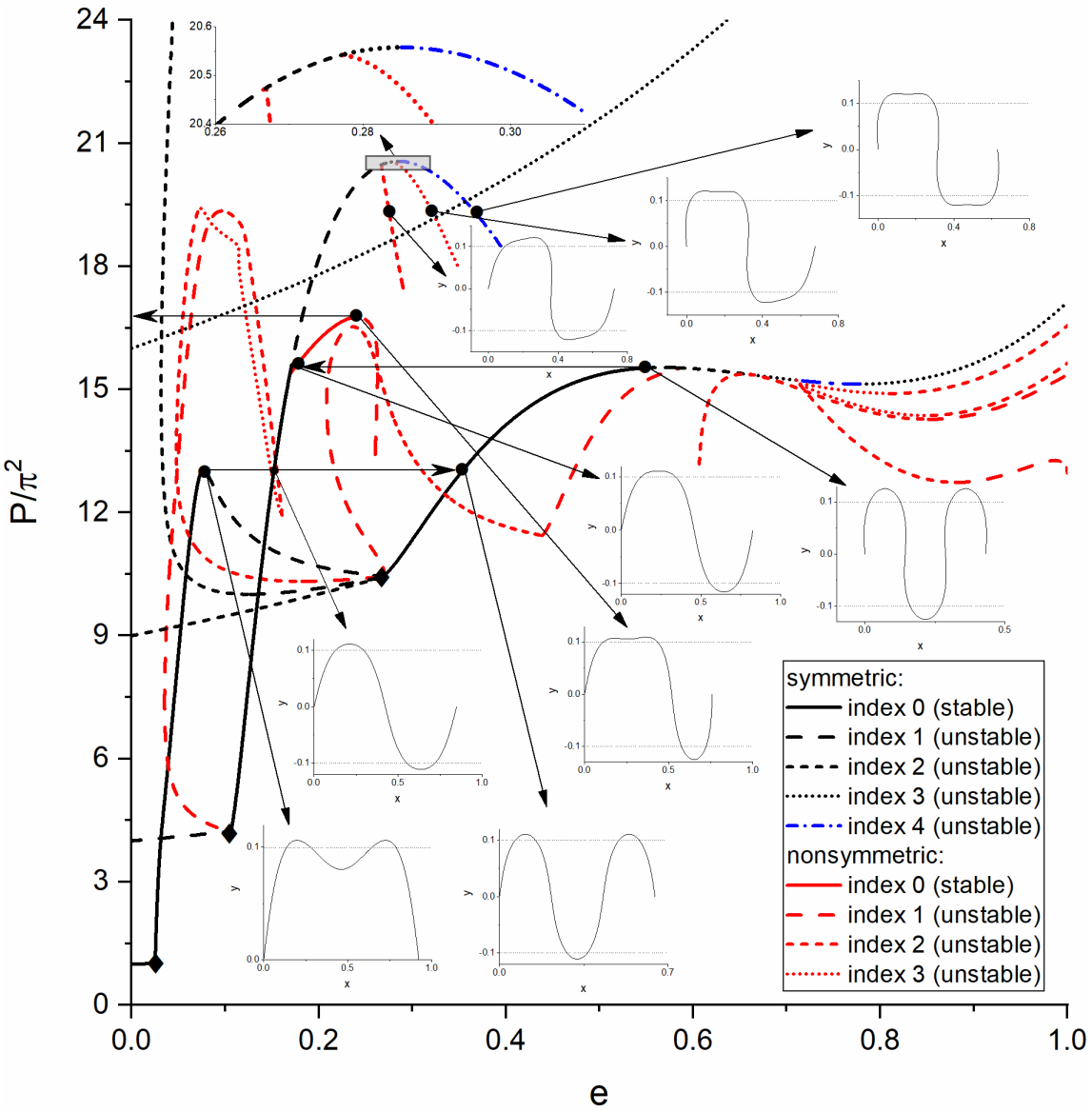

Fig. 9 Bifurcation diagram with stability indicated. Diamonds label points of first wall contact. Dynamical jumps are indicated by horizontal arrows. ($h = 0.1,\ \beta = 10^5$.)

symmetry is retained. Finally, after a further increase of P, just before the maximum is reached, the solution loses all symmetry.

The complicated bifurcation behaviour along the continuing third-mode branch is resolved in the enlargement shown in Fig. 10. We again see various types of symmetry-breaking, now also occurring in stages. From the bifurcation seen at $e = 0.66$ emerge two branches of symmetry-broken solutions that are still reflection-symmetric. On both sides of this bifurcation (at $e = 0.59$ and $e = 0.71$) are symmetry-breaking bifurcations with emerging branches of solutions with broken reflection symmetry. The one on the right, however, generates solutions that are sheared but otherwise remain symmetric, with congruent half waves. The inset at $e = 0.8$ along this branch illustrates this by showing solutions from both (superimposed) branches coming out of the (supercritical) pitchfork bifurcation. Earlier along this branch there is a second-stage symmetry-breaking in which these sheared solutions lose all symmetry.

The bifurcation at $e = 0.66$ and the second-stage bifurcation are instances of a new type of, seemingly higher-order, bifurcation not encountered before. As clarified by the zooms in the figure, they are characterised by: (i) tangency of two continuing branches, and (ii) no exchange of stability when going across. Whether acting as first- or second-stage symmetry-breaking bifurcation, these 'tangent' bifurcations have in common that they break congruence of the half waves. It is interesting to note that all bifurcating branches in Fig. 10 carry different type of symmetry-broken solutions and that all types of symmetry-breaking seem to be present.

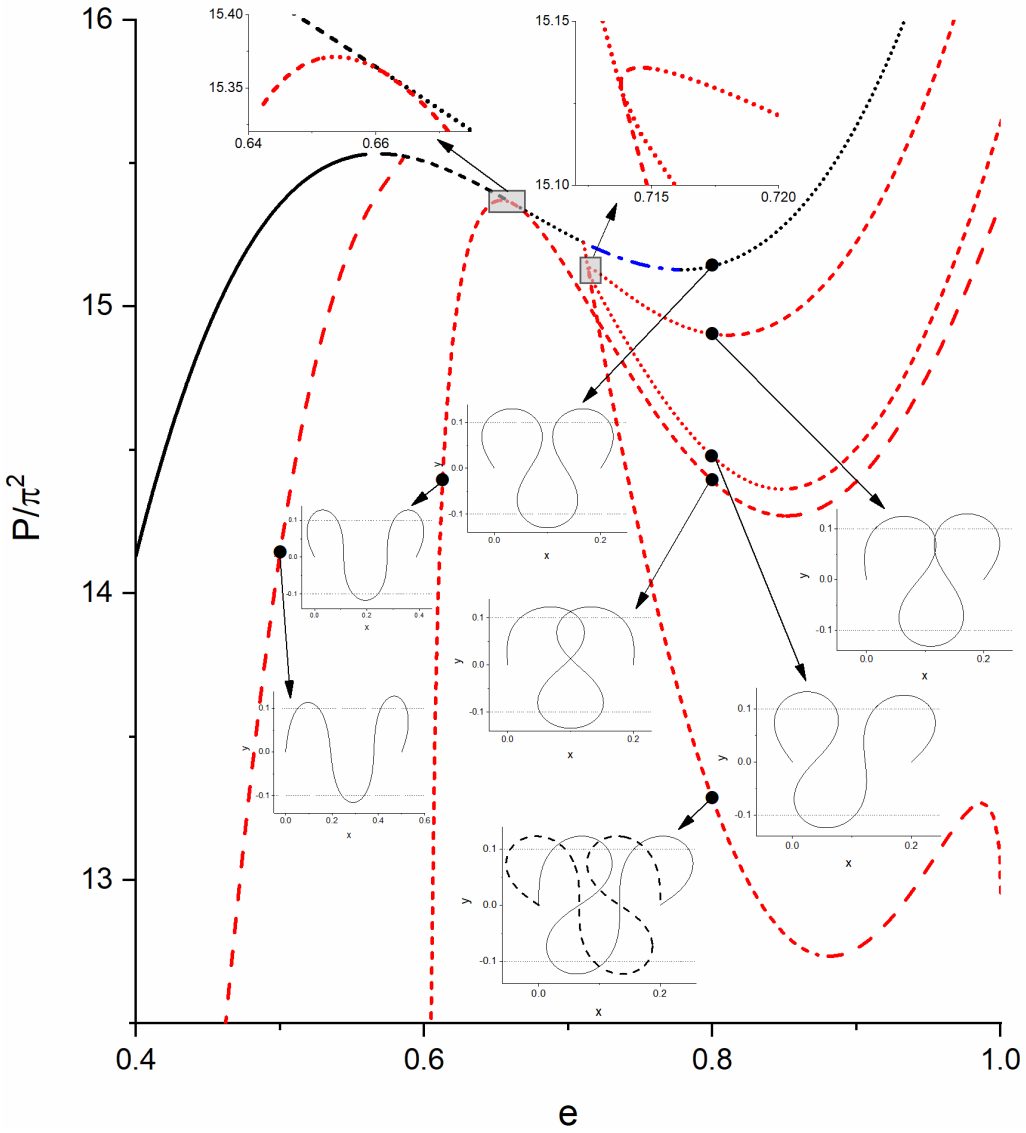

Fig. 10 Enlargement of Fig. 9 showing different stages of symmetry-breaking along the third-mode branch. ($h = 0.1,\ \beta = 10^5$.)

The sequence of events near the third-mode contact point is particularly complicated and a blow-up of the region, with solution insets, is shown in Fig. 11. Several subcritical symmetry-breaking bifurcations eventually lead (via index 2, then index 1, then index 0) to the stabilisation of the third mode. We analyse this stabilisation process further in Section 5. Fig. 12 illustrates how, coming from the stable branch at large P, stability is lost when entering the index-1 region. The figure shows $x(s),\ y(s) + \varepsilon Y(s)$ for several values of ε, where Y is the eigenfunction corresponding to the sole eigenvalue $\mu = 0.8544$ in [0,1]. The plot reveals that the instability is of the type of branch `f' in Fig. 11.

As another example, Fig. 13 shows the complete bifurcation diagram for $h = 0.16$. This value is larger than h_3, so no contacting third-mode solution is available, and, although $h < h_2$, no stable second-mode solution is available either when the first-mode loses stability at the maximum in P. We conclude that the rod jumps from this maximum, at $P = 9.6968\pi^2$, directly into the straight tensile state, as indicated by the horizontal arrow. Bifurcations along the second-mode branch show another case of two-stage symmetry-breaking illustrated in the figure by insets at $e = 0.64$ and $e = 1$. Along the lowest of the three branches going through $e = 1$, symmetry is broken by shearing, while overall (point) symmetry, and hence congruence of the half waves, is retained (analogous to events along the third-mode branch in Fig. 10). The inset at $e = 0.64$ illustrates this by showing solutions from both (superimposed) branches coming out of the (subcritical) pitchfork bifurcation. At $e = 1$ all these second-mode solutions form figures-of-eight. The lowest of these is rotated just the right amount to fit

between the walls with two point contacts and zero contact force. This solution, reached at $P = 6.4287\pi^2$, is therefore given by the Euler elastica. It satisfies

$$\frac{x(1/4)}{y(1/4)} = \frac{F_y}{P} = \tan\varphi_2,$$

with $\varphi_2 = 0.7435$ the (clockwise) angle rotated from the vertical (and determined by the value of h). As indicated in Fig. 13, this solution is stable before closing at $e = 1$ at which point the solution goes unstable due to a rigid-body mode of rotation. The solution branch of this rigid-body rotation in the bifurcation diagram is the vertical line $e = 1$ down from $P = 6.4287\pi^2$. Along this branch, φ_2 increases monotonically, reaching $\varphi_2 = \pi/2$ when $P = 0 = y(1/4)$.

There is a second branch of stable nonsymmetric solutions in Fig. 13, going through $P = 0$. This means that the corresponding solution, shown in the figure, can be held by zero force. At slightly positive load ($P = 0.2759\pi^2$) this solution closes into a loop (half figure-of-eight) at $e = 1$, at which point it becomes unstable due to a rigid-body mode. The solution at this point is again rotated such as to be described by the Euler elastica and satisfies

$$\frac{x(1/2)}{y(1/2)} = \frac{F_y}{P} = \tan\varphi_1,$$

with $\varphi_1 = 1.4441$ the angle from the vertical. Along the bifurcating vertical branch $e = 1$ of rigid-body rotations this angle reaches $\pi/2$ when $P = 0 = y(1/2)$. There are two more first-mode solutions at $P = 0$, both unstable: an index-1 nonsymmetric solution and an index-2 symmetric solution. Fig. 14 illustrates the instability caused by the three corresponding linear modes.

As a final example, Fig. 15 gives the bifurcation diagram for $h = 0.2$. This value is only slightly lower than h_2 and consequently there is only a small branch of stable contacting second-mode solutions. Nevertheless, the jump from the first-mode at the fold is to this second-mode. Under further increase of the load this is then quickly followed, at $P = 7.4366\pi^2$, by a final jump into the straight tensile state.

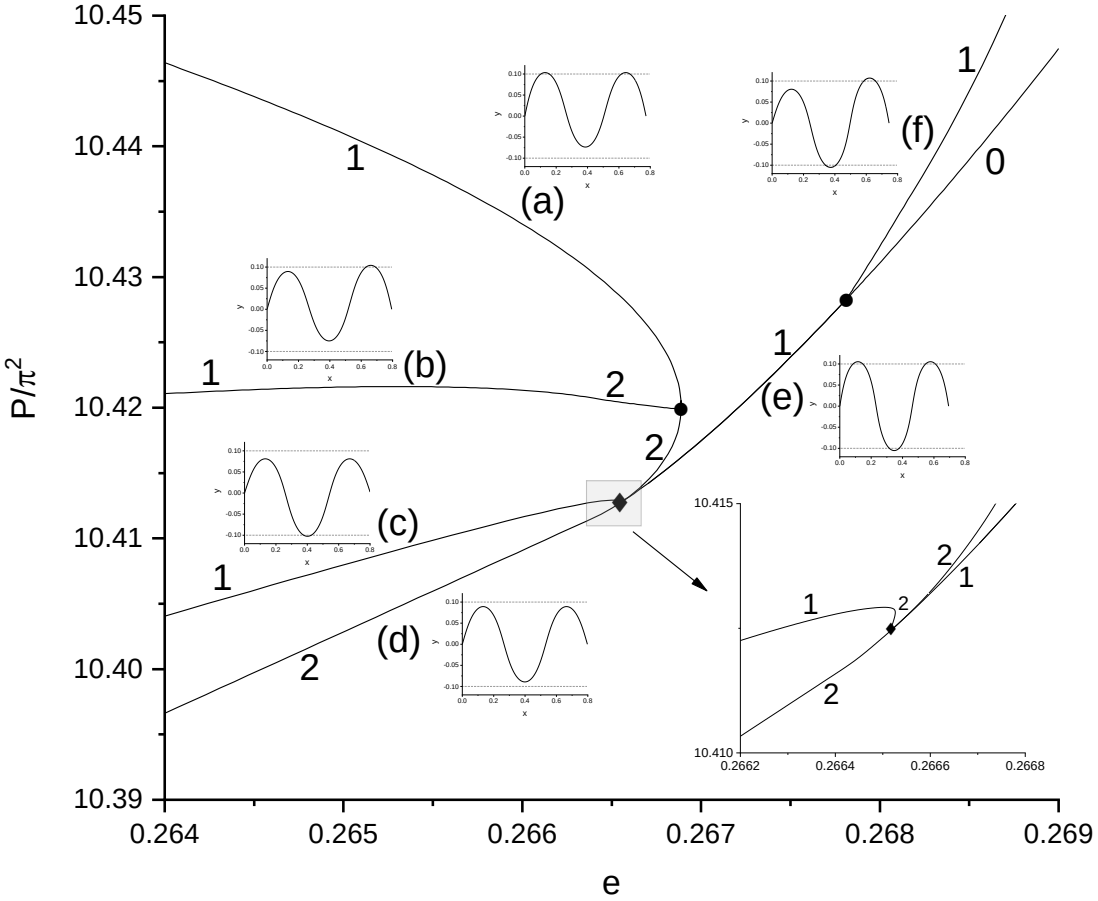

Fig. 11 Enlargement of the third-mode contact region in Fig. 9. The stability index is indicated along the solution branches. Note that all bifurcations are subcritical pitchforks. ($h = 0.1,\ \beta = 10^5$.)

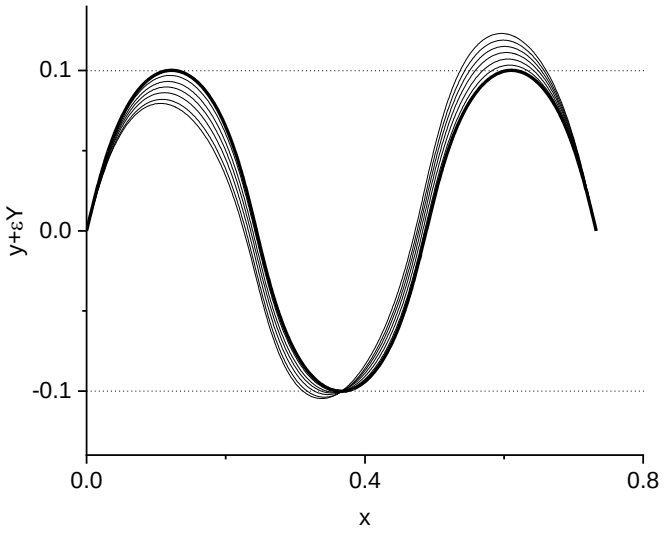

Fig. 12 Unstable mode of the index-1 solution at $(e,P) = (0.2675,\ 10.4240\pi^2)$ along branch 'e' in Fig. 11.

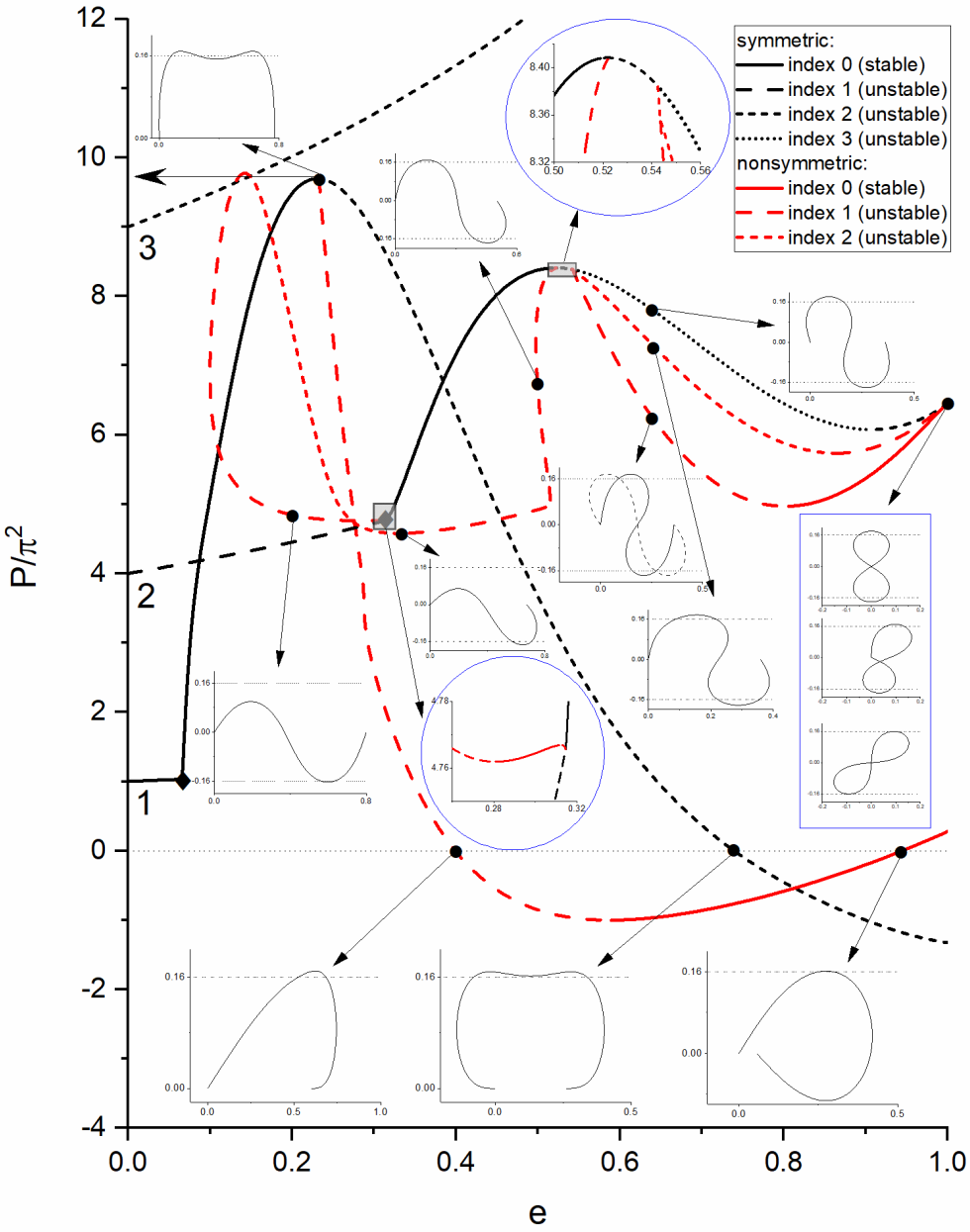

Fig. 13 Bifurcation diagram with stability indicated. Diamonds label points of first wall contact. ($h = 0.16,\ \beta = 10^5$.)

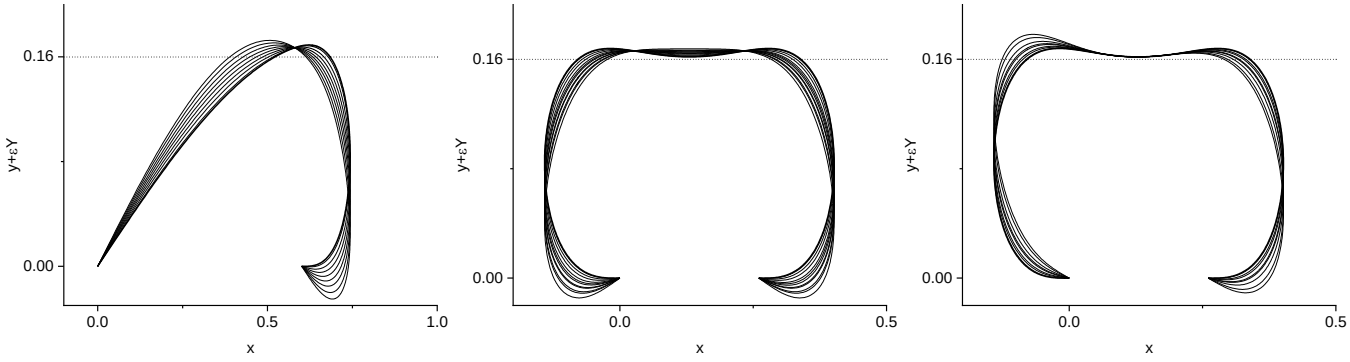

(a) (b) (c)

Fig. 14 Unstable modes of the unstable solutions at $P = 0$ displayed in Fig. 13.

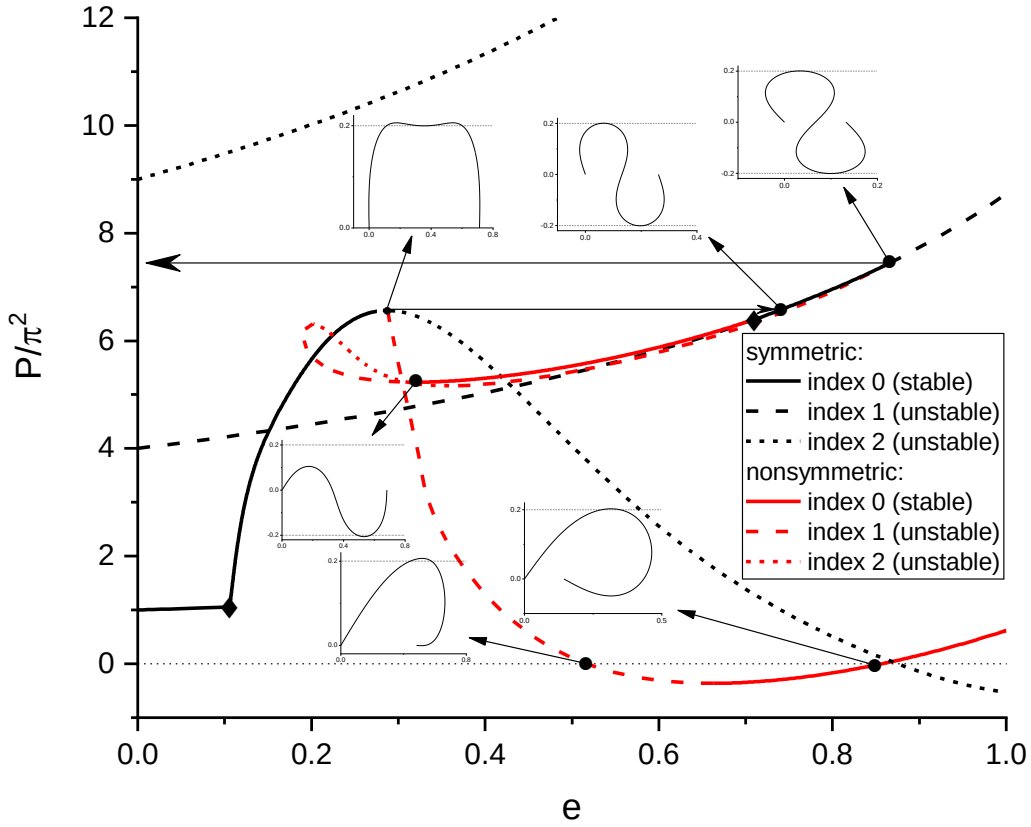

Fig. 15 Bifurcation diagram with stability indicated. Diamonds label points of first wall contact. Dynamical jumps are indicated by horizontal arrows. ($h = 0.2,\ \beta = 10^5$.)

5. Contact combinatorics – routes to modal stabilisation

It is well known that for the free elastica all modes higher than the first are unstable. Since constraints generally have the effect to stabilise solutions, it is natural to suppose that stable higher modes touching both walls may exist in this soft-contact problem. In the hard-contact case this is indeed what has been observed in experiments (Domokos et al., 1997; Roman and Pocheau, 2002). It is good to realise though that contact of a higher-mode elastica with *parallel* walls is initially made at multiple points. The stability of such configurations is not entirely straightforward; the image of a four-legged chair comes to mind. Indeed, higher elastica modes are not just unstable, they are multiply unstable with increasingly higher degree of instability (stability index) as the mode number goes up. Now, in standard (smooth) bifurcations the index changes only by one. Stabilisation of higher modes therefore requires a succession of such bifurcations to obtain a stable solution (in the hard contact case a degenerate bifurcation could result in a change of index by more than one). This is exactly what we are finding in our detailed bifurcation diagrams in Figs 9, 13 and 15. Here we take a closer look at the organisation of all these bifurcations in this modal stabilisation.

The enlargement in Fig. 11 shows the successive stages of stabilisation for third-mode contact. In the first bifurcation, in which contact is first made, the index changes from 2 to 1, while in the second bifurcation the index is further lowered to 0 resulting in a stable solution. The first bifurcation (a subcritical pitchfork) involves only branches of left-right reflection-symmetric solutions. Solutions along the two bifurcating branches are, however, up-down symmetry-broken. All four types of solutions involved are therefore physically distinct, so there are four distinct branches in the (e,P) diagram (they have different numbers of free and contacting half waves, so their e values are different). The second bifurcation, by contrast, is a left-right symmetry-breaking bifurcation (again a subcritical pitchfork). Solutions on its two bifurcating branches are merely reflected but otherwise physically the same (in particular, they have the same number of free and contacting half waves), so only one bifurcating curve, 'f', appears in the (e,P) diagram. There is a further left-right symmetry-breaking bifurcation occurring along the incoming 'a' branch, creating 'b'. The six branches involved in third-mode contact represent all possible combinations with each of the three half waves either losing wall contact or staying in contact with (and burrowing into) the wall (see Fig. 11).

We conjecture that this pattern (which also covers second-mode contact) is repeated at higher modes. We can succinctly encode solutions involved in the various bifurcations by writing '+' for a contacting half wave and '−' for a free half wave. The solutions in Fig. 11 can then be represented by the binary symbol sequences $+-+$, $--+$, $-+-$, $---$, $+++$ and $-++$, in that order.

To aid the classification of solutions we introduce the following terminology. The **opposite** of a string of symbols is the string with all $+$ symbols changed to $-$ and vice versa. The **inverse** of a string is the string obtained by reading symbols in reverse order. Thus, taking the case $n = 3$ again, establishing 3-point contact, in the first contact bifurcation, means going from the **uniform** string $---$ to its opposite $+++$. The left-right symmetric solutions involved in this bifurcation form a pair of opposite palindromic strings. Such pairs of palindromic strings, that can similarly appear together in pitchfork bifurcations, are listed for a few higher modes in Fig. 16. We call such pitchfork bifurcations **symmetri**c. All these individual palindromic strings correspond to physically distinct solutions on separate branches. Pairs of inverse strings, on the other hand, correspond to a single solution curve in the (e,P) bifurcation diagram coming out of a left-right symmetry-breaking bifurcation. We call such pitchfork bifurcations **nonsymmetric**.

Note that these symbol strings nicely capture the essence of the nodal patterns. They do not distinguish between 'buckled-up' and 'buckled-down' solutions and are also insensitive to the difference in the precise nature of the reflection symmetry, i.e., line symmetry for odd modes against point symmetry for even modes (cf. Fig. 16).

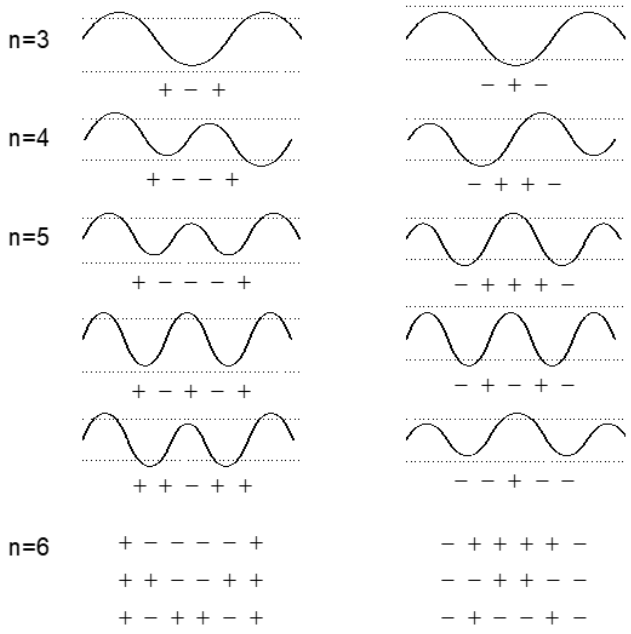

Fig. 16 All nonuniform pairs of opposite palindromic solutions appearing together in symmetric pitchfork bifurcations for the first six modes.

Assuming that all contact/non-contact combinations are involved in n-mode contact, we can predict the number of solution curves to be expected in bifurcation diagrams. The total number of strings of n symbols is 2^n. For the number of curves involved in symmetric bifurcations we need to calculate the number of palindromic strings of n symbols. For the additional branches coming out of nonsymmetric bifurcations we need to calculate the number of *pairs* of inverse strings of n symbols. Let

$$o_n := (\#\text{ pairs of opposite palindromes of } n \text{ symbols}) = 2^{\left[\frac{n-1}{2}\right]}$$

$$i_n := (\#\text{ pairs of inverse strings of } n \text{ symbols}) = \frac{2^n - 2o_n}{2} = 2^{n-1} - 2^{\left[\frac{n-1}{2}\right]}$$

where $[x]$ denotes the integer part of x. We then have

$$b_n := (\#\text{ bifurcations, either symmetric or nonsymmetric, involved in contact}) = o_n + i_n - 1 = 2^{n-1} - 1$$

$$c_n := (\#\text{ distinct bifurcation curves in } (e,P) \text{ diagram near contact}) = 2o_n + i_n = 2^{n-1} + 2^{\left[\frac{n-1}{2}\right]}$$

Note here that o_n includes the pair of trivial uniform strings of all $+$ and all $-$, representing the through branch, for which the -1 in b_n corrects.

Table 1 gives numbers for the first 6 modes. Numbers are minimal numbers required for all contact patterns to be present as in principle multiple, or reverse, bifurcations could occur (although we have not found such instances). For $n = 3$ we find 3 bifurcations and 6 solution branches, in agreement with Fig. 11 (and with numerical results in (Domokos et al., 1997)). Numbers for $n = 1$ and $n = 2$ also agree with the bifurcation diagrams in Figs 9, 13 and 15 (including 0 bifurcations required for the first mode). For larger n the number of bifurcations and distinct solution branches are going up rapidly. We note that in counting the number of curves, c_n, it is assumed that opposite palindromic pairs with equal numbers of symbols $+$ and $-$ in each member of the pair (for instance, $+--+$ and $-++-$ for $n = 4$, see Fig. 16) and non-opposite palindromic strings with equal numbers of symbols $+$ and $-$ (for instance $++--++$ and $+-++-+$ for $n = 6$) nevertheless correspond to physically different solutions on distinct solution branches in the (e,P) plane. This seems reasonable for finite solutions that have boundary conditions to satisfy.

Table 1 Numbers of binary symbol strings and bifurcation curves for the first six modes n

n	o_n	i_n	b_n	c_n
1	1	0	0	2
2	1	1	1	3
3	2	2	3	6
4	2	6	7	10
5	4	12	15	20
6	4	28	31	36

In linear theory contacting solutions are constructed from segments of free linearised elastica solutions and segments of contacting solutions of a beam on a linear elastic foundation. All higher modes are stable. They simply have nowhere to go: there are no nonsymmetric solutions (Domokos et al., 1997) and a half wave cannot grow at the expense of a neighbouring wave, the way the free elastica loses stability (this is confirmed by direct stability calculations for the linear Eq. (9)). One therefore expects an n-mode to be stable for sufficiently small h in the nonlinear theory as well. Numerical calculations show indeed that a stable fourth mode, with 4-point contact, exists for $h = 0.05$ at (e,P)=(0.12, 176.36). Stabilisation of a general n-mode, with n-point contact, requires $n - 1$ bifurcations along the uniform through branch $--...---$, $++...+++$. These can in principle be any of the b_n available bifurcations, either symmetric or nonsymmetric (note that $b_n \geq n - 1$ for all n). For $n = 3$ (at $h = 0.1$) these are the single symmetric bifurcation and one of the two nonsymmetric bifurcations (with the second nonsymmetric bifurcation acting as a *secondary* bifurcation along a bifurcated branch, spawning branch 'b' in Fig. 11). It is good to realise that this could have been different, for instance two nonsymmetric bifurcations could have caused the index change, and this may indeed be the case for other parameter values. For $n = 4$ stabilisation may be achieved by the single symmetric bifurcation (cf. Fig. 16) followed by one of the $i_4 = 6$ nonsymmetric bifurcations. For higher modes

there are many possible scenarios and one would have to do a numerical bifurcation study to find out which route to stabilisation is taken for given physical parameters.

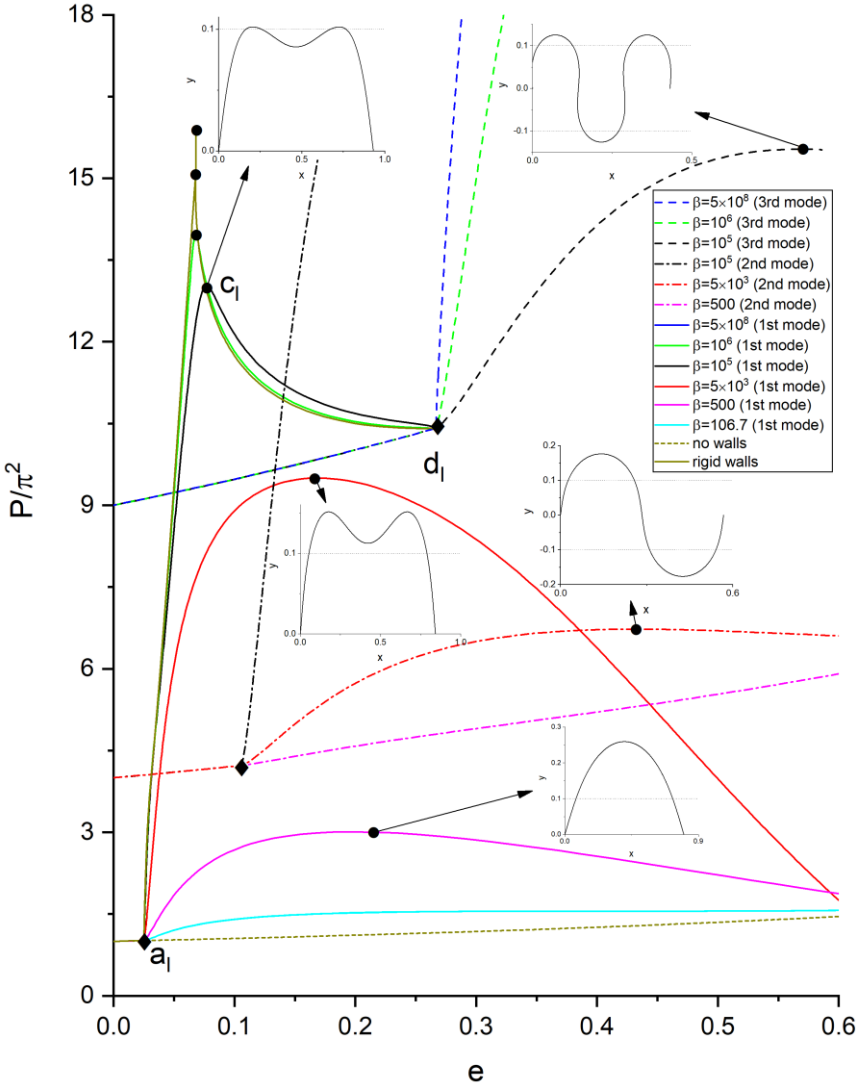

Fig. 17 (Partial) bifurcation diagrams for different values of β focussing on the first-mode peak value of P ($h = 0.1$).

6. Effect of the wall stiffness β

We have taken the value $\beta = 10^5$ for the wall stiffness throughout. Here we briefly study the dependence of the initial jump from the first mode on β. Partial bifurcation diagrams for various values of β are displayed in Fig. 17. Only symmetric branches are shown. For the largest value, $\beta = 5 \times 10^8$, the bifurcation curve approaches the sharp hard-contact result obtained from the linear analysis in ((Feodosiev, 1977), Problem 121), also included in the figure. As β is lowered wall contact becomes increasingly less important. For $\beta = 5000$ the stabilisation picture is still largely intact: the second and third modes are stabilised through a single symmetry-breaking bifurcation and two successive bifurcations respectively, as in Fig. 9. However, the maximum along the first-mode branch does not reach high enough anymore to enable a jump into the third mode. No second mode is available either at that load so the rod will jump from the first mode into the straight tensile state. A closer look reveals a critical value $\beta_3 = 7336$: no jump into the third mode is possible for $\beta < \beta_3$. A jump into the second mode is similarly impossible once β has dropped below $\beta_2 = 838$. These critical values are superficially similar to the critical h_i in Section 3, but, unlike those h_i, they are not obtained analytically and they are not universal as they depend on the value of h.

For $\beta = 500$ the wall is too soft to stabilise the second mode. There is still a maximum along the first-mode branch, but, as the inset shows, the solution is hardly affected by the wall: the rod does not deflect inwards anymore. The first-mode

maximum finally disappears at $\beta = 107.6$, at the point $(e,P) = (0.388689, 1.5525\pi^2)$. For lower values of β the loading curve essentially follows the free elastica curve. The solution remains stable up to the point where the ends meet ($e = 1$) at $P = 4\mathrm{K}(k_1)^2 = 2.1834\pi^2$, where k_1 solves $2E(k) - K(k) = 0$, with instability caused by a rigid-body rotation (Kuznetsov and Levyakov, 2002).

7. Discussion

We have presented results of a bifurcation study of the soft-contact problem in which a rod is compressed, and buckled, between two parallel elastic walls. The observed behaviour depends strongly on the distance between the walls, $2h$ (or, in dimensional terms, on the slenderness ratio h/L, where L is the length of the rod). The smaller h, the more buckling modes can be supported; for large h the rod simply becomes too short to bounce the requisite number of times back and forth between the two walls (critical values, h_n, proportional to $1/n$, for arbitrary mode number n, have been obtained analytically from elastica theory). As a result, for smaller h, the bifurcation behaviour becomes more and more complicated with various interactions between modes, either gradually via symmetry-breaking bifurcations, or suddenly via dynamic jumps at folds. The physical interpretation of the multiple solutions requires a stability analysis to assess which are stable and therefore likely to be observed in practice. To aid this interpretation of complicated bifurcation diagrams we have developed a new stability method based on numerical bifurcation theory.

Our stability method is essentially the adjacent equilibrium method, well known from elastic stability theory, but applied here successively to record the stability index. The adjacent equilibrium method is not usually applied in succession probably because once a solution has gone unstable it is not of great interest anymore. If, as in our case, the bifurcation diagram is very complicated, however, with various modal interactions, then solutions that have gone unstable may later be stabilised. (This is different from the free elastica where there is no modal interaction and all modes evolve separately.) It would be very challenging in the current problem to identify the stable branches without stability information. Pitchfork bifurcations may be sub- or supercritical with implications for the (relative) stability of the solution branches involved. Whichever is the case is not clear from simply looking at the branches. Indeed, several of our solution curves were only discovered after stability calculations revealed a change of stability index along a branch where a bifurcation had been missed (for instance the branch of stable nonsymmetric second-mode solutions in Fig. 9 and several of the bifurcating third-mode branches at larger e in the same figure).

The numerical method is found to perform very well. The index calculations confirm that all bifurcations encountered (except the 'tangent' bifurcations in Fig. 10) are generic sub- or supercritical pitchfork bifurcations with standard exchange of stability, although in some cases this requires quite accurate numerics to resolve small-scale features (for instance near the third-mode contact point zoomed into in Fig. 11). The results agree with the hard-contact experiments in (Domokos et al., 1997) and qualitatively with numerical results, based on conjugate point theory, for a similar soft-wall buckling problem in (Manning and Bulman, 2005).

This success of our method is despite two challenging features of the system under study. The first is a nonsmoothness typical of contact problems involving touch-down. Since this contact is soft, the wall compliant, the nonsmoothness (discontinuity) is only in the second derivative of F_y (and the first derivative of f_y), not the first derivative F_y, as in hard contact (cf. Eq. (5) and Fig. 4). By comparison, buckling problems such as those considered in (Manning and Bulman, 2005) do not involve touch-down and are infinitely smooth. The second complicating factor is the large relative stiffness of the walls, β. This introduces a large (or small) parameter in the equations making them singularly perturbed, thereby complicating the numerics. The large value of β is responsible for the noted small-scale bifurcation features; notice that the turn along one of the solution branches in the inset in Fig. 11 is roughly on the scale of $1/\beta$.

At initial wall contact of the third-mode elastica solution all three half waves simultaneously touch the wall. We find that in soft contact this degenerate situation is resolved by a sequence of pitchfork bifurcations generating a complete set of solutions in which, upon further compression, each half wave can either burrow into or recede from the wall. The various contact profiles can therefore be characterised by binary strings of three symbols. Assuming that the same pattern holds for general n-modes, we can use string combinatorics to count the number of expected pitchfork bifurcations, b_n, and distinct

solution curves, c_n, in load-deflection bifurcation diagrams in the neighbourhood of initial n-mode contact. This allows us to propose scenarios for the successive stabilisation of higher modes, but numerical bifurcation studies are required to verify these.

As to this stabilisation of higher modes, the following picture emerges (at least for sufficiently large β). In the linear theory (valid in the limit $h \to 0$) infinitely many (stable) modes exist. In the nonlinear large-deformation theory (valid for finite h) for any h, no matter how small, only a finite number of modes exist (since only a finite number of h_n are larger than this h). For any n, a stabilised n-mode exists for small enough h, after the requisite number $n-1$ of index changes effected by $n-1$ pitchfork bifurcations along the through branch coming out of the elastica critical point at $P = n^2\pi^2$. These $n-1$ bifurcations are among b_n bifurcations near initial contact, involving c_n curves of solutions with different contact patterns, i_n of which are nonsymmetric. All b_n bifurcations coalesce in the hard contact limit $\beta \to \infty$. All nonsymmetric solutions, connecting different modes, are 'squeezed out' in the limit $h \to 0$ as the linear theory does not admit nonsymmetric solutions. Note the scale on which these contact stabilisation phenomena take place: the contacting n-mode comes into existence only for $h < h_n = \mathrm{O}(1/n)$ and all nonsymmetric versions of it, generated in symmetry-breaking bifurcations, have to disappear in the limit $h \to 0$.

Under increasing P these stable higher modes (symmetric or nonsymmetric) may be reached after successive dynamic jumps from lower modes. Eventually, however, since there are only a finite number of stable contact modes (and non-contacting higher modes are unstable), the rod is 'pushed through' to the straight tensile state, the only stable solution left. As h is increased fewer and fewer modes can be maintained at contact and 'push through' happens at lower compressive loads P. When $h > h_1 = 0.4031$ even the first mode cannot reach contact and the jump into the straight state occurs when the ends of the rod coincide ($e = 1$) at $P = 4\mathrm{K}(k_1)^2 = 2.1834\pi^2$.

Free pinned-pinned elastica modes are self-similar in the sense that higher modes are multiple copies of the (rescaled) first mode. Each of these half waves is itself reflection-symmetric and therefore liable to undergo symmetry-breaking. As a special case, individual half waves may lose symmetry in such a way that overall reflection-symmetry of the mode is retained. We see such events along the second- and third-mode branches in Figs 9, 10 and 13. Some of these events are associated with the exceptional higher-order congruence-breaking 'tangent' bifurcations, as seen along the third-mode branch in Fig. 10. Further higher-order bifurcations will likely occur along branches of even higher modes as there are various ways such modes may break congruence. All these symmetry-breaking bifurcations seem to require relatively large compressive loads P that push the rod firmly into the wall (indeed, they generally occur near P maxima). They do therefore not interfere with the rich set of contact phenomena described in Section 5, which occur around initial contact at relatively modest P.

The various (nonlinear) symmetry-breaking phenomena uncovered here are expected to be universal and to occur widely in compressed elastic structures subject to lateral resistance other than hard or soft contact. These phenomena include multi-stage symmetry-breakings of higher-mode deformations. Example systems include rods or sheets under external force fields due to surface tension, electric or magnetic fields or deforming on an elastic foundation or in a surrounding soft matrix, for instance as models for polymers or biological structures (Brangwynne et al., 2006; Brau et al., 2011) (all solutions in Fig. 10 can be continued periodically so all congruence-breaking bifurcations are equivalent to period-doubling bifurcations in the dynamical view adopted in (Brau et al., 2011)).

There are several cases in our analysis where multiple solutions are available when a jump under dead loading must take place at a local maximum of P. This is for instance the case in Fig. 9 at the maximum along the first-mode branch. Comparing the solution at this maximum with the stable solutions available along the second- and third-mode branches, one might guess that the jump would take place to the third-mode solution, which seems 'closer', but it is hard to know what is the relevant 'metric' here. It would be interesting to do experiments to investigate which jump would take place in practice, or simulations using the dynamics equations.

Acknowledgments

ZW would like to acknowledge funding by the National Natural Science Foundation of China (grant number 52001229).

References

Alderliesten, T., Konings, M.K., Niessen, W.J., 2006. Modeling friction, intrinsic curvature, and rotation of guide wires for simulation of minimally invasive vascular interventions. IEEE Transactions on Biomedical Engineering 54 (1), 29-38.

Antman, S.S., 1995. Nonlinear Problems of Elasticity. Springer-Verlag, Berlin.

Brangwynne, C.P., MacKintosh, F.C., Kumar, S., Geisse, N.A., Talbot, J., Mahadevan, L., Parker, K.K., Ingber, D.E., Weitz, D.A., 2006. Microtubules can bear enhanced compressive loads in living cells because of lateral reinforcement. J Cell Biol 173 (5), 733-741.

Brau, F., Vandeparre, H., Sabbah, A., Poulard, C., Boudaoud, A., Damman, P., 2011. Multiple-length-scale elastic instability mimics parametric resonance of nonlinear oscillators. Nature Physics 7 (1), 56-60.

Brush, D.O., Almroth, B.O., 1975. Buckling of Bars, Plates, and Shells. McGraw-Hill.

Chai, H., 1998. The post-buckling response of a bi-laterally constrained column. Journal of the Mechanics and Physics of Solids 46 (7), 1155-1181.

Chanane, B., 2015. Eigenvalues of vectorial Sturm-Liouville problems with parameter dependent boundary conditions. Abstract and Applied Analysis 2015, 796086.

Chen, J.-S., Chen, D.-W., 2019. Deformation of a spatial elastica constrained inside a springy tube. Acta Mechanica 230 (12), 4303-4310.

Chen, J.-S., Hung, S.-Y., 2014. Deformation and stability of an elastica constrained by curved surfaces. International Journal of Mechanical Sciences 82, 1-12.

Chen, J.-S., Wen, Z.-S., 2019. Deformation and vibration of a buckled beam constrained by springy walls. European Journal of Mechanics - A/Solids 77, 103791.

Doedel, E.J., Oldeman, B.E., et al., AUTO-07P: Continuation and Bifurcation Software for Ordinary Differential Equations (Concordia University, 2019) (the latest version of the code is available from http://cmvl.cs.concordia.ca/auto).

Domokos, G., Holmes, P., Royce, B., 1997. Constrained Euler buckling. Journal of Nonlinear Science 7 (3), 281-314.

Feodosiev, V.I., 1977. Selected Problems and Questions in Strength of Materials. Mir, Moscow.

Gao, D.L., Huang, W.J., 2015. A review of down-hole tubular string buckling in well engineering. Petroleum Science 12 (3), 443-457.

Gilbertson, M.D., McDonald, G., Korinek, G., Van de Ven, J.D., Kowalewski, T.M., 2017. Serially actuated locomotion for soft robots in tube-like environments. IEEE Robotics and Automation Letters 2 (2), 1140-1147.

Katz, S., Givli, S., 2015. The post-buckling behavior of a beam constrained by springy walls. Journal of the Mechanics and Physics of Solids 78, 443-466.

Kuznetsov, V.V., Levyakov, S.V., 2002. Complete solution of the stability problem for elastica of Euler's column. International Journal of Non-Linear Mechanics 37 (6), 1003-1009.

Love, A.E.H., 1892. A Treatise on the Mathematical Theory of Elasticity. Cambridge University Press.

Manning, R.S., 2009. Conjugate points revisited and Neumann–Neumann problems. SIAM Review 51 (1), 193-212.

Manning, R.S., Bulman, G.B., 2005. Stability of an elastic rod buckling into a soft wall. Proceedings of the Royal Society A: Mathematical, Physical and Engineering Sciences 461 (2060), 2423-2450.

Manning, R.S., Rogers, K.A., Maddocks, J.H., 1998. Isoperimetric conjugate points with application to the stability of DNA minicircles. Proceedings of the Royal Society of London. Series A: Mathematical, Physical and Engineering Sciences 454 (1980), 3047-3074.

Pryce, J.D., 1993. Numerical Solution of Sturm-Liouville Problems. Oxford University Press.

Roman, B., Pocheau, A., 2002. Postbuckling of bilaterally constrained rectangular thin plates. Journal of the Mechanics and Physics of Solids 50 (11), 2379-2401.

Sattinger, D., 1971. Stability of bifurcating solutions by Leray-Schauder degree. Archive for Rational Mechanics and Analysis 43 (2), 154-166.

Tan, X., Forsman, B., 1995. Buckling of slender string in cylindrical tube under axial load: experiments and theoretical analysis. Experimental Mechanics 35 (1), 55-60.

van der Heijden, G.H.M., 2001. The static deformation of a twisted elastic rod constrained to lie on a cylinder. Proceedings of the Royal Society A 457 (2007), 695-715.

van der Heijden, G.H.M., Neukirch, S., Goss, V.G.A., Thompson, J.M.T., 2003. Instability and self-contact phenomena in the writhing of clamped rods. International Journal of Mechanical Sciences 45 (1), 161-196.

Wang, H., Yamamoto, A., 2017. Analyses and solutions for the buckling of thin and flexible electrostatic inchworm climbing robots. IEEE Transactions on Robotics 33 (4), 889-900.

Yeh, C.-Y., Chou, S.-C., Huang, H.-W., Yu, H.-C., Juang, J.-Y., 2019. Tube-crawling soft robots driven by multistable buckling mechanics. Extreme Mechanics Letters 26, 61-68.